

Structure-Composition-Property Relationships in Antiperovskite Nitrides

Hongxia Zhong^{1#}, Chunbao Feng^{2#}, Hai Wang³, Dan Han⁴, Guodong Yu¹, Wenqi Xiong¹,
Yunhai Li¹, Mao Yang^{5,6}, Gang Tang^{7*}, and Shengjun Yuan^{1*}

¹School of Physics and Technology, Wuhan University, Wuhan, 430072, People's Republic
of China

²School of Science, Chongqing University of Posts and Telecommunications, Chongqing
400065, China

³School of Mathematics and Physics, China University of Geosciences (Wuhan), Wuhan
430074, China

⁴Department of Chemie, Ludwig-Maximilians-Universität München, München, 81377,
Germany

⁵Institut für Physik and IRIS Adlershof, Humboldt-Universität zu Berlin, Berlin 12489,
Germany

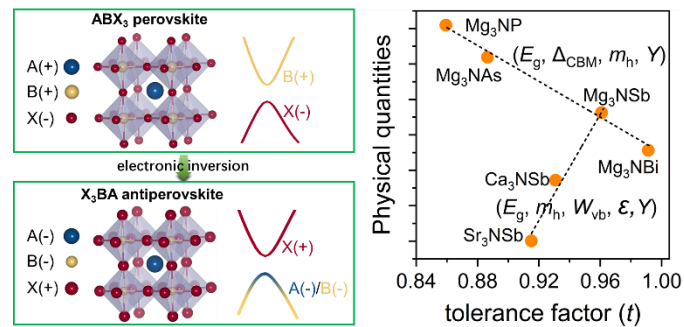
⁶School of Science, Xi'an Polytechnic University, Xi'an 710048, P. R. China

⁷Theoretical Materials Physics, Q-MAT, CESAM, University of Liège, B-4000 Liège,
Belgium

Abstract

ABX₃ perovskites have attracted intensive research interest in recent years due to their versatile composition and superior optoelectronic properties. Their counterparts, antiperovskites (X₃BA), can be viewed as electronically inverted perovskite derivatives, but they have not been extensively studied for solar applications. Therefore, understanding their composition-property relationships is crucial for future photovoltaic application. Here, taking six antiperovskite nitrides $X_3^{+2}N^{3-}A^{3-}$ (X = Mg, Ca, Sr; A = P, As, Sb, Bi) as an example, we investigate the effect of X- and A-sites on the electronic, dielectric, and mechanical properties from the viewpoint of the first-principles calculations. Our calculation results show that the X-site dominates the conduction band, and the A-site has a non-negligible contribution to the band edge. These findings are completely different from traditional halide perovskites. Interestingly, when changing X- or A-site elements, a linear relationship between the tolerance factor and physical quantities, such as electronic parameters, dielectric constants, and Young's modulus, is observed. By designing the Mg₃NAs_{1-x}Bi_x alloys, we further verify this power of the linear relationship, which provides a predictive guidance for experimental preparation of antiperovskite alloys. Finally, we make a comprehensive comparison between the antiperovskite nitrides and conventional halide perovskites for pointing out the future device applications.

TOC GRAPHICS



Introduction

Perovskite semiconductors have attracted intensive research interest in recent years due to their versatile compositions and tunable electronic and optical properties.¹⁻³ As an important member in the perovskite family, lead (Pb) halide perovskites $APbX_3$ ($A^+ = CH_3NH_3^+$, $CH(NH_2)_2^+$, Cs^+ ; $X^- = I^-, Br^-, Cl^-$) have achieved great success of applications in solar cells,¹ light-emitting diodes,² and photodetectors (Figure 1).³ For example, the power conversion efficiency (PCE) of perovskite solar cells has been rapidly improved from 3.8% to 25.5% within only one decade.^{4,5} Despite the exciting progress, long-term instability and Pb toxicity are still key challenges hindering perovskite solar cells from practical applications.⁶

Over the past decade, great efforts have been devoted to explore Pb-free and stable perovskite alternatives. Two classes of potential materials have been picked up, which are $ASnX_3$ single perovskites and $A_2M(I)M(III)X_6$ ($M^+ = In^+, TI^+$; $M^{3+} = Sb^{3+}, Bi^{3+}$) double perovskites. $ASnX_3$ shows the similar crystal structure and electronic properties to its Pb counterparts, but suffers from the serious instability issues (i.e., against the oxidation to Sn^{4+}).⁷ $A_2M(I)M(III)X_6$ double perovskites have been predicted theoretically to be isoelectronic with $APbX_3$.⁸ Unfortunately, TI^+ is more toxic than Pb^{2+} , and In^+ -based double perovskites tend to be unstable against oxidation or form mixed-valence compounds with distorted and complex crystal structures.⁹⁻¹¹

Chalcogenide perovskites ABX_3 ($A^{2+} = Ca^{2+}, Sr^{2+}, Ba^{2+}$; $B^{4+} = Ti^{4+}, Zr^{4+}, Hf^{4+}$; $X^{2-} = S^{2-}, Se^{2-}$) with robust thermal stability and nontoxic elements were proposed as potential photovoltaic absorbers (Figure 1).^{12,13} Due to the large electronegativity difference between B- and X-site ions and the disorder in ground state structure, they usually exhibit a large band gap, and they are difficult to form high-quality films at low temperatures.¹² Although the experimentally synthesized $Ba_3Zr_2S_7$ posses a surprisingly optimal band gap of 1.28 eV,¹⁴ the calculated band structure shows that its valence band maximum (VBM) and conduction band minimum (CBM) do not exhibit sufficient dispersion (i.e., small band width W and large carrier effective mass m). Therefore, it is very challenging to realize the well-performed solar cell based on chalcogenide perovskites.

In addition to conventional perovskites ABX_3 , some researchers began to pay attention to their counterparts, antiperovskites (X_3BA),¹⁵⁻¹⁸ in which the B anions are located in the center of 6-fold coordinated octahedra and the A anions are 12-fold coordinated with the X cations (Figure 1). Recently, Gebhardt *et al.* proposed a series of inverse-hybrid perovskites $(CH_3NH_3)_3BA$ (B: monovalent anions, A: divalent anions or B: divalent anions, A: monovalent anions). Unfortunately, these compounds still do not have the dispersive valence and conduction bands near the Fermi level.^{15, 19} On the contrary, several reported all-inorganic antiperovskite semiconductors X_3NA ($X^{2+} = Ca^{2+}, Mg^{2+}$; $A^{3-} = P^{3-}, Sb^{3-}, Bi^{3-}$) possess suitable direct band gaps and high optical absorption coefficients, indicating that they are promising photovoltaic absorbers.^{17, 18, 20} Exploring the composition-property relationships are very important for understanding and designing photovoltaic materials with excellent performance.²¹ For conventional ABX_3 perovskites, it is well known that the B- and X-site anions have major impacts on the electronic structures, while A-site cation does not contribute the band edge because of its highly ionic nature.²² But the composition-property relationship in antiperovskites has not been fully understood.²¹

In this work, we study the electronic, dielectric, and mechanical properties of antiperovskite X_3NA ($X^{2+} = Mg^{2+}, Ca^{2+}, Sr^{2+}$; $A^{3-} = P^{3-}, As^{3-}, Sb^{3-}, Bi^{3-}$) based on first-principles calculations. Our calculation results show that both X- and A-sites affect the electronic properties near the Fermi level significantly. With varying X and A composition, the antiperovskite X_3NA undergoes an indirect to direct band gap transition, and the composition-property has been analyzed deeply. Importantly, we further find that the composition-property relationship can be well rationalized by a simple geometric parameter, tolerance factor. When changing X- or A-site element, a general linear relationship between the tolerance factor and physical qualities, including electronic parameters, dielectric constants, and Young's modulus, is uncovered. The linear relationship can be further verified in the antiperovskite nitride alloys. Finally, we make a comprehensive comparison between the antiperovskite nitrides and conventional lead halide perovskites. Our studies will provide a guideline to design favorable antiperovskite nitrides for different applications.

Results and Discussions

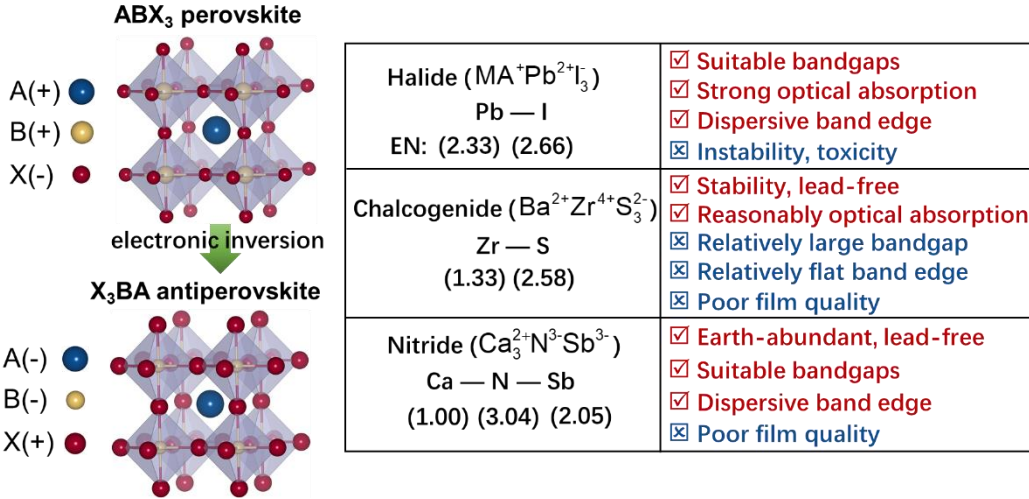


Figure 1: Crystal structures of cubic perovskite ABX_3 and antiperovskite X_3BA . Three representatives, lead halide perovskite, chalcogenide perovskite, and antiperovskite nitride, are presented, with their corresponding preponderances and disadvantages. The electronegativities (EN) of the elements are given in parentheses.

As shown in Figure 1, through electronically inverting the formula ABX_3 (A and B are cations, and X is an anion), a class of antiperovskite X_3BA can be obtained, in which anions occupy the A and B sites, and cations occupy the X sites. Generally, for a polar-covalent semiconductor, anions mainly contribute to VBM, and cations dominate CBM. Therefore, the exchange of the positions of the anions and cations may change electronic characteristics of VBM and CBM. Here, we focus on antiperovskite nitrides ($B = N^{3-}$), in which the moderate electronegativity of the N atom ($\chi_N = 3.0$) (comparable to Cl ($\chi_{Cl} = 3.2$), but less than O ($\chi_O = 3.5$) and F ($\chi_F = 4.0$)) gives rise to unique properties.²³ In order to explore the composition-property relationship, we vary the A-site element from Mg^{2+} to Sr^{2+} , and the X-site element from P^{3-} to Bi^{3-} . The optimized lattice constants of X_3NA ($X^{2+} = Mg^{2+}, Ca^{2+}, Sr^{2+}; A^{3-} = P^{3-}, As^{3-}, Sb^{3-}, Bi^{3-}$) are summarized in Table 1.

Goldschmidt's tolerance factor t is an important geometric parameter to describe the structure stability of perovskite materials. For X_3NA antiperovskites, t is defined as $t = (r_X + r_A)/[\sqrt{2}(r_X + r_N)]$, where r_X , r_A , and r_N are the ionic radii of X^{2+} , A^{3-} and N^{3-} ions (see Table

S1), respectively. The estimated t for X_3NA ($X^{2+} = Mg^{2+}, Ca^{2+}, Sr^{2+}$; $A^{3-} = P^{3-}, As^{3-}, Sb^{3-}, Bi^{3-}$) is summarized in Table 1. Generally, a conventional cubic perovskite crystal likely exists if $0.85 \leq t \leq 1.0$,¹⁶ and a smaller t represents other lower symmetry structures.¹⁶ Therefore, the calculated t values indicate that the studied six antiperovskites X_3NA may be stable in a cubic structure. We also check the phase stability of the chosen antiperovskite X_3NA , and seven representative phases $Pm\bar{3}m$, $Pbnm$, $P6_3/mmc$, $Pnma$, $R\bar{3}c$, $R\bar{3}$, and $P6_3/cm$ are considered (see Figure S1). The calculated results are consistent with previous reports.^{20, 24} The cubic $Pm\bar{3}m$ phase is found to be the most stable structure with the lowest total energies for antimonides and bismuthides, which can be also proved by the non-imaginary phonon spectrum (see Figure S3). Although the theoretically predicted ground state phases of Mg_3NP and Mg_3NAs are the orthorhombic $Pbnm$, cubic Mg_3NAs has been synthesized successfully.²⁵ For Mg_3NP , the calculated total energies of orthorhombic $Pbnm$ and rhombohedral $R\bar{3}c$ are about 10 meV/atom lower than that of cubic $Pm\bar{3}m$. Considering that the nitride antiperovskites are fabricated at high temperatures (~ 800 °C), cubic $Pm\bar{3}m$ Mg_3NP may be stabilized by temperature, since the energy difference is smaller than 38 meV/atom.¹¹ In the following discussions, we focus on understanding the changing trend of physical properties of cubic $Pm\bar{3}m$ antiperovskites X_3NA ($X^{2+} = Mg^{2+}, Ca^{2+}, Sr^{2+}$; $A^{3-} = P^{3-}, As^{3-}, Sb^{3-}, Bi^{3-}$).

Table 1: Calculated lattice constant a , Goldschmidt's tolerance factor t , band gap E_g , static dielectric constant ϵ_{std} , exciton binding energy E_b , and optical transition features between band edges at Γ point for X_3NA ($X^{2+} = Mg^{2+}, Ca^{2+}, Sr^{2+}$; $A^{3-} = P^{3-}, As^{3-}, Sb^{3-}, Bi^{3-}$) antiperovskites.

Compound	a (Å)		t	E_g (eV)	ϵ_{std}	E_b (meV)	Optical transition
	Calc.	Expt.					
Mg_3PN	4.178		0.859	2.480	45.399	65	Allowed
Mg_3AsN	4.236		0.886	2.119	36.130	12	Allowed
Mg_3SbN	4.375	4.217	0.961	1.235	31.567	10	Allowed
Mg_3BiN	4.437	4.382	0.991	0.696	38.919	4	Allowed
Sr_3SbN	5.214	5.173	0.915	0.905	41.695	14	Allowed
Ca_3SbN	4.873	4.854	0.931	1.025	32.752	12	Allowed

To explore the composition-property relationship, we first replace the X-site element in X_3NSb ($X^{2+} = Sr^{2+}, Ca^{2+}, Mg^{2+}$) and calculate their band structures and partial density of states

(PDOSs) by HSE06+SOC method (see Figure S4), which are shown in Figure 2. It can be seen that the predicted band gap trend is $E_g(\text{Sr}_3\text{NSb}) < E_g(\text{Ca}_3\text{NSb}) < E_g(\text{Mg}_3\text{NSb})$ (see Table 1). More importantly, we find that the electronic-band dispersions of Sr_3NSb and Ca_3NSb are analogous, but which are very different from that of Mg_3NSb . Like prototype MAPbI_3 , Sr^{2+} and Ca^{2+} -based antiperovskites show suitable direct band gaps and very dispersive bands near the band edges. But Mg_3NSb exhibits an indirect band gap with VBM located at the Γ point and CBM located at the M point. Previous and our results indicate that the valence band width of Mg_3NSb is larger than those of Sr_3NSb and Ca_3NSb . This is because²⁰ the p - p hybridization ($\text{Mg}3p$ - $\text{N}2p$ and $\text{Mg}3p$ - $\text{Sb}5p$) in Mg_3NSb is stronger than the d - p hybridization ($\text{Sr}/\text{Ca}d$ - $\text{N}2p$ and $\text{Sr}/\text{Ca}d$ - $\text{Sb}5p$) in Sr_3NSb and Ca_3NSb (see Figure 2). But the large difference in CBM (composed of X^{2+} states) is ignored in these literatures. When X-site element changes from Sr to Ca to Mg, M_c and Γ_c states move downward and upward, respectively, and the CBM finally moves from Γ to M point in Mg_3NSb . Further, we analyze the variation of the two states by the orbital contribution at the two states, as shown in Table 2. For M_c states, the X-site contribution changes from higher energy $\text{Sr}/\text{Ca}d$ orbitals in X_3NSb ($\text{X}^{2+} = \text{Sr}^{2+}$ and Ca^{2+}) to lower $\text{Mg}3s$ orbitals Mg_3NSb . As a result, the M_c state is pulled down as the X-site element changes from Sr to Ca to Mg. While the higher Γ_c state is caused by the enhanced orbital overlap between X^{3-} and Sb^{3-} in Mg_3NSb , which is consistent with the PDOS in Figure 2. This heightened orbital overlap generally correlates with the smaller X-Sb bond length. Here, we define quantitatively the energy difference between the two conduction states Γ_c and M_c point as Δ_{CBM} ,²⁶ and the value of Δ_{CBM} decreases from 1.858 eV in Sr_3NSb to 1.696 eV in Ca_3NSb , to -0.214 eV in Mg_3NSb (Table 2). The negative Δ_{CBM} indicates a direct to indirect band gap transition in antiperovskites. Interestingly, this similar direct to indirect transition has also been observed in two-dimensional crystals from Si_3O to C_3O .²⁷

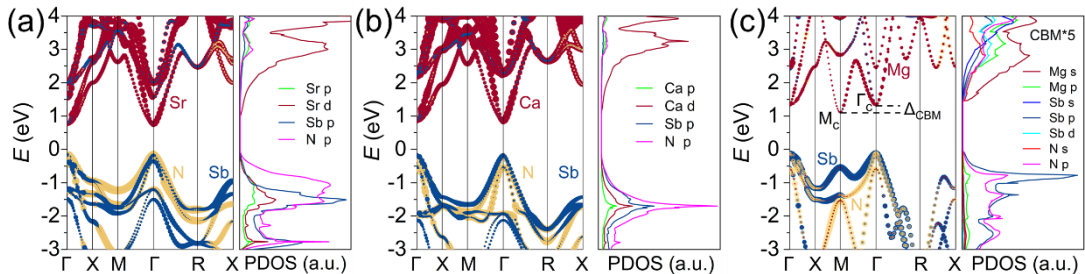


Figure 2: Electronic band structures and partial density of states (PDOSs) of cubic

antiperovskite for (a) Sr_3NSb , (b) Ca_3NSb , and (c) Mg_3NSb . All bands are shifted to align the deep Sb 4s band. For clarity, the negligible orbital contributions to the PDOSs are not shown here. Two lowest conduction band states M_c and Γ_c , and the energy difference between the two states (Δ_{CBM}) are labelled in (c).

Table 2: The percent contributions from each atomic orbital to the two conduction band states M_c and Γ_c in $X_3\text{NSb}$ ($X^{2+} = \text{Sr}^{2+}, \text{Ca}^{2+}, \text{Mg}^{2+}$).

Compound	Δ_{CBM} (eV)	M_c			Γ_c		
		X (%)	B	N	X	B	N
Sr_3SbN	1.858	50(s)+13(p)+21(d)	10(d)	6(s)	13(s)+82(d)	5(d)	0
Ca_3SbN	1.696	44(s)+7(p)+30(d)	11(d)	8(s)	11(s)+83(d)	6(d)	0
Mg_3SbN	-0.214	63(s)+2(p)	10(d)	25(s)	70(s)+13(d)	17(d)	0

From the PDOS of Mg_3NSb , it can be observed that the 5p states of A-site Sb³⁻ anion also contribute to the VBM, which is very different from the conventional halide perovskites. To further clarify the effects of A-site on the electronic structure, we construct a hypothetical frame model $[\text{Mg}_3\text{N}]^{3+}$ with Sb³⁻ ions removed in the same crystal lattice (see Figure S5) and calculate its band structure. Surprisingly, the system turns out to be a metal after removing all Sb atoms, which is quite different from the original semiconducting Mg_3NSb , further confirming the significant contributions of A sites to the electronic structure in antiperovskites. On the contrary, in conventional halide perovskites, the band structure of $[\text{PbI}_3]^-$ model without Cs⁺ ions is almost the same as that of the original CsPbI_3 (see Figure S5), indicating that the A-site cations do not affect the electronic states around the band edge. Further, electron localization function (ELF) analyses identify the partial covalent nature of A-X bond (ELF ~ 0.8), which is very dissimilar to the typical ionic bond (i.e., Cs-I) in the inorganic halide perovskites (see Figure S6). Therefore, we expect to substitute A-site elements to further tune the Δ_{CBM} in Mg_3NA ($\text{A}^{3-} = \text{P}^{3-}, \text{As}^{3-}, \text{Bi}^{3-}$), as shown in Figure 3. It can be seen that the band-edge dispersions of all Mg-based antiperovskites are very similar. The predicted band gap trend is $E_g(\text{Mg}_3\text{NBi}) < E_g(\text{Mg}_3\text{NSb}) < E_g(\text{Mg}_3\text{NAs}) < E_g(\text{Mg}_3\text{NP})$. Interestingly,

when replacing Sb^{3-} with a heavier element (i.e., Bi^{3-}), $|\Delta_{\text{CBM}|}$ becomes larger. However, when Sb^{3-} is replaced with lighter elements (i.e., As^{3-} and P^{3-}), the value of Δ_{CBM} changes from negative to positive, suggesting that the direct band gap is restored. In addition, the high valley degeneracy is observed in Mg-based antiperovskites. For example, the VBM at Γ valley ($N_k = 1$) has four (six) fold orbital degeneracy ($N_o = 4$ (6)) for Mg_3NP and others, leading to the corresponding band degeneracy of $N_v = 4$ (6).²⁸ And the CBM has two valleys Γ and M , with the valley degeneracy $N_E > 1$.²⁹ Therefore, all the Mg-based nitride antiperovskites may serve as high performance thermoelectric materials as revealed by previous studies.²⁴

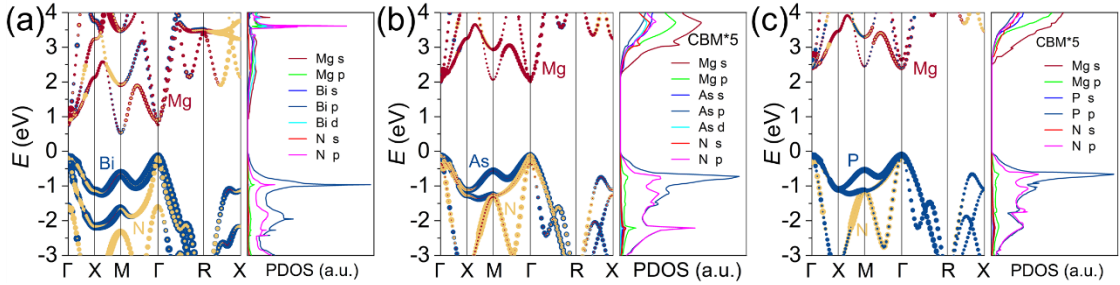


Figure 3: Electronic band structures and partial density of states (PDOSs) of the cubic $Pm\bar{3}m$ phase antiperovskite for (a) Mg_3NBi , (b) Mg_3NAs , and (c) Mg_3NP . The top of the valence band is set to zero.

To rationalize the changing trend of the electronic properties, we summarize some physical quantities (i.e., E_g , Δ_{CBM} , m_h , w_{vb}) as functions of the tolerance factor (t) for X_3NA ($\text{X}^{2+} = \text{Mg}^{2+}, \text{Ca}^{2+}, \text{Sr}^{2+}$; $\text{A}^{3-} = \text{P}^{3-}, \text{As}^{3-}, \text{Sb}^{3-}, \text{Bi}^{3-}$) in Figure 4. When replacing X-site element with larger ionic radius (i.e., from Mg^{2+} to Ca^{2+} to Sr^{2+}), as the value of t decreases, band gap (E_g), average hole effective mass (m_h), and valence band width (w_{vb}) decrease. More importantly, a positive linear relationship between $E_g/m_h/w_{vb}$ and t is observed in Figure 4. This is because that the s/d levels of X-site go down in energy from Mg^{2+} to Sr^{2+} (see Figure S7), pulling down the CBM and reducing the band gap. We note that a similar linear relationship has already been theoretically and experimentally reported in traditional inorganic halide perovskite alloys.^{30,31} If substituting A-site element with larger ionic radius (i.e., from P^{3-} to

As³⁻ to Sb³⁻ to Bi³⁻), as the value of t increases, E_g , Δ_{CBM} , and m_h decrease. And a negative linear relationship between $E_g/\Delta_{\text{CBM}}/m_h$ and t is observed, which can be explained by the fact that the p levels increase monotonously (see Figure S7), which pushes up the VBM and reduces the band gap accordingly. Meanwhile, the p - p hybridization becomes stronger, resulting in larger W_{vb} and smaller m_h for A-site element in group VA. Surprisingly, we find that regardless of the replacement of A-site or X-site, the Δ_{CBM} shows a negative linear dependence on the t , as a consequence of lower s orbitals of Mg and Bi elements.

A large static dielectric constant provides strong screening, thereby suppressing carrier scattering, trapping, and recombination, eventually improving transport properties.³² We next focus on the static dielectric constants of $X_3\text{NA}$ ($X^{2+} = \text{Mg}^{2+}, \text{Ca}^{2+}, \text{Sr}^{2+}$; $\text{A}^{3-} = \text{P}^{3-}, \text{As}^{3-}, \text{Sb}^{3-}, \text{Bi}^{3-}$), and summarize the results in Table S3 and Figure 4e. The values of the static dielectric constant range from 31.57 in Mg_3NSb to 45.40 in Mg_3NP , comparable to those of the halide perovskites (see Table S3).³³ The value of Mg_3NSb is in line with previous report.¹⁷ Further, we decompose the static macroscopic dielectric tensor to ionic (ε_{ion}) and electronic (ε_{ele}) contributions separately, and focus on the ε_{ele} , which is related with the electronic properties directly. A positive linear relationship between ε_{ele} and t is clearly observed for Mg_3NA ($\text{A}^{3-} = \text{P}, \text{As}, \text{Sb}, \text{Bi}$). With increasing t , the ε_{ele} increases from 9.37 at $t = 0.86$ in Mg_3NP to 20.63 at $t = 0.99$ in Mg_3Nbi . This is attributed to the linear relationship between band gap and tolerance factor in Figure 4a, because a larger band gap generally leads to a smaller ε_{ele} .³⁴ On the other hand, we find that the ε_{ele} is not sensitive to the X-site element. Based on the calculated ε_{ele} , we estimate the exciton binding energies E_b of the six studied anti-perovskites $X_3\text{NA}$ (see Table 1). Mg_3NP has the largest E_b of 65 meV, as a result of its largest effective mass and smallest electronic dielectric constant. The estimated E_b for other five $X_3\text{NA}$ ranges from 4 meV to 14 meV (see Table 1), smaller than the thermal energy ($(k_{\text{B}}T \sim 26$ meV) at room temperature. The small exciton binding energy will facilitate rapid electron-induced carrier dissociation, which is considerably important for an ideal solar cell absorber.

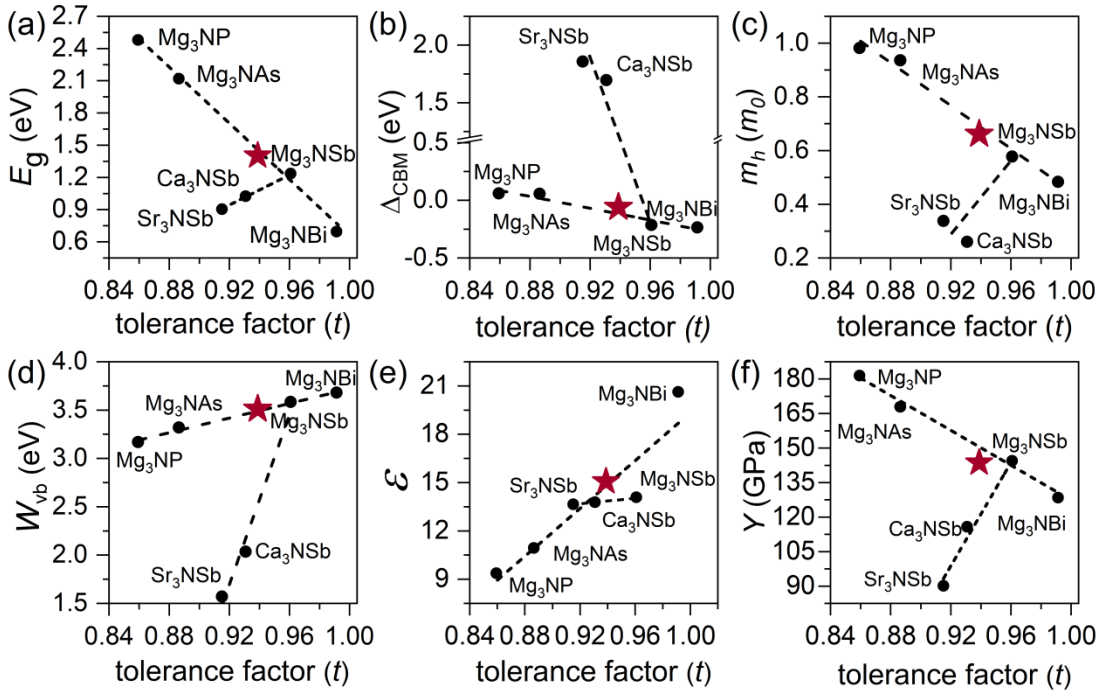


Figure 4: (a) Band gaps (E_g), (b) energy difference between the two conduction states at Γ and M point (Δ_{CBM}), (c) average hole effective mass (m_h), (d) valence band width (W_{vb}), (e) electronic dielectric constant (ϵ), (f) Young's module (Y) for cubic $Pm\bar{3}m$ phase X_3NA ($X^{2+} = Mg^{2+}, Ca^{2+}, Sr^{2+}$; $A^{3-} = P^{3-}, As^{3-}, Sb^{3-}, Bi^{3-}$) antiperovskites. The red stars show the corresponding data for $Mg_3NAs_{0.5}Bi_{0.5}$ alloy.

For the practical fabrication and device applications, the mechanical properties of materials are very important and they can be useful to predict their aging behaviors. We thus summarize the calculated elastic constants of all the studied antiperovskites X_3NA in Table S5. The dependence of the derived Young's modulus (Y) on tolerance factor (t) is shown in Figure 4f. A similar linear relationship is clearly identified between Y and t . For instance, for the Mg-based nitride compounds, the Y value declines monotonously with increasing t when changing the A-site in Group VA. The Y value decreases from 181.48 GPa at $t = 0.86$ in Mg_3NP to 128.49 GPa at $t = 0.99$ in Mg_3NBi . While for the X_3NSb , the Y value increases monotonously with increasing t when replacing the X-site in Group II, ranging from 90.10 GPa at $t = 0.915$ in Sr_3NSb to 144.46 GPa at $t = 0.99$ in Mg_3NSb . This linear variation of Young's modulus can be related to the N-X bond length in X_3NA (see Figure S8), where smaller bond length generally requires large strain to break out, leading to large Y . More importantly, all the

cubic antiperovskites X_3AN are found to be brittle with negative Cauchy and $B/G \leq 1.75$ in Figure S9, while halide perovskites $CsPbX_3$ ($X = Cl, Br, I$) are ductile. Therefore, the antiperovskites X_3AN possess a low probability to develop flexible devices.

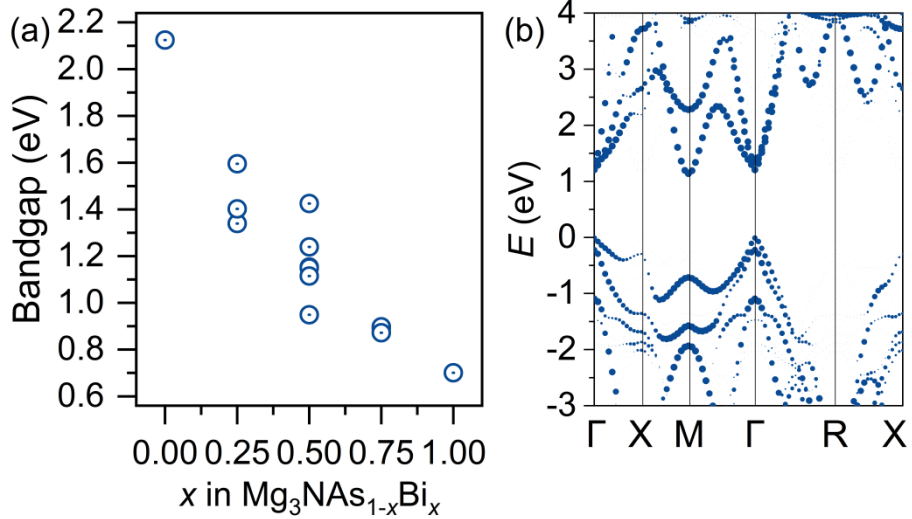


Figure 5: (a) Calculated band gaps of $Mg_3NAs_{1-x}Bi_x$ as a function of x , the amount of Bi. (b) The unfolded band structures of $Mg_3NAs_{0.5}Bi_{0.5}$ in the most stable configuration.

The alloys strategy has been proven to be an effective way to modify the properties of perovskites and overcome some disadvantages of single compounds,³⁵ and The trends discussed before are very instructive for the design of alloys. Here, we investigate the band gaps of $Mg_3NAs_{1-x}Bi_x$ alloys with $x = 0.0, 0.25, 0.50, 0.75$, and 1.00 (see Figure S10), which may possess an ideal band gap (~ 1.5 eV) for single-junction solar cells based on the linear relationship in Figure 4a. It is shown that although the band gap differs between different configurations for a certain x , the band gap of $Mg_3NAs_{1-x}Bi_x$ alloys generally decreases with increasing x , reduced from 2.102 eV in Mg_3NAs to 0.612 eV in Mg_3NBi (see Figure 5a). This decreasing trend is associated with the higher Bi- p orbitals than As- p orbitals.

Finally, in order to validate the practicability of the linear rule, we focus on $Mg_3NAs_{0.5}Bi_{0.5}$ in the most stable configuration. The tolerance factor of this alloy is 0.94. Figure 5b shows the band structure with the bands unfolded back from super-cell to its primitive unit cell, which can be comparable with the bands of primitive cell, and quantitative analysis of alloy is

enabled.³⁶ It clearly shows a quasi-direct band gap of 1.402 eV. This data has been added as star sign in Figure 4a, located at the fitted line, confirming the linear rule in band gap again. This is another confirmation that we can use this rule to design antiperovskites with optimal band gap (~ 1.5 eV) for solar cells. Furthermore, the Δ_{CBM} , m_h , and w_{vb} of $\text{Mg}_3\text{NAs}_{0.5}\text{Bi}_{0.5}$ are -0.061 eV, 0.661 m_0 , and 3.510 eV, agreeing well with the predicted data of -0.059 eV, 0.685 m_0 , and 3.591 eV, respectively, using the linear relationship in Figures 4b-d. For dielectric constants of $\text{Mg}_3\text{NAs}_{0.5}\text{Bi}_{0.5}$, they are isotropic in x and y directions, but a little anisotropic in z direction. The ε_{ele} (ε_{ion}) is around 15.06 (23.00) in Table S3. Finally, the Young's modulus for $\text{Mg}_3\text{NAs}_{0.5}\text{Bi}_{0.5}$ is 143.61 GPa. Both the ε_{ele} and Y are on the fitting lines in Figures 4e-f. Thus, the physical quantities of $\text{Mg}_3\text{NAs}_{0.5}\text{Bi}_{0.5}$ alloy confirm the linear relationship in antiperovskite nitrides in Figure 4. We can use this universal relationship to design suitable antiperovskites for different optoelectronic applications.

Toward future practical application, let us now make a comprehensive comparison between antiperovskite nitrides X_3NA ($\text{X}^{2+} = \text{Mg}^{2+}, \text{Ca}^{2+}, \text{Sr}^{2+}$; $\text{A}^{3-} = \text{P}^{3-}, \text{As}^{3-}, \text{Sb}^{3-}, \text{Bi}^{3-}$) and the widely studied three-dimensional (3D) lead-halide perovskites APbX_3 ($\text{A}^+ = \text{MA}^+, \text{FA}^+, \text{Cs}^+$; $\text{X}^- = \text{Cl}^-, \text{Br}^-, \text{I}^-$) (see Figure 6). Overall, X_3NA possess very similar electronic and optical properties as those of APbX_3 , such as suitable band gaps (~ 1.5 eV), small carrier effect masses (0.26-0.98 m_0), small exciton binding energies (4-65 meV), and allowed optical transitions at band edges. Compared with APbX_3 , the antiperovskites X_3NA are obtained by electronically inverting the formula, resulting in totally different band-edge characteristics. More interestingly, the effect of the A-site element on the electronic structure has a non-negligible effect in the antiperovskites, which is quite different from the halide perovskites. In addition, according to the predicted mechanical properties, antiperovskites are difficult to be applied in flexible devices in the future. On the other hand, compared with the simple low-temperature solution processing of halide perovskites, most of the antiperovskites synthesized in current experiments are powder samples, which are prepared at high temperatures, such as Mg_3NAs and Mg_3NSb .^{17,25} Therefore, although the successful synthesis of the antiperovskites films in experiment has been reported, the preparation of high-quality films is still challenging, which

is a key step for future device application.

Figure 6: A comprehensive comparison of 3D antiperovskite X_3BA and the typical 3D halide perovskite ABX_3 for band structure, electronic bandgap E_g , exciton binding energy E_b , carrier effective mass m_h , optical transition character, Young's modulus Y , softness, synthesis method, and sample type.

	3D antiperovskite X_3BA	3D halide perovskite ABX_3
Crystal structure		
Material example	$A^{3-} = P^{3-}, As^{3-}, Sb^{3-}, Bi^{3-}$ $B^{3-} = N^{3-}$ $X^{2+} = Mg^{2+}, Ca^{2+}, Sr^{2+}$	$A^+ = MA^+, FA^+, Cs^+$ $B^{2+} = Pb^{2+}$ $X^- = Cl^-, Br^-, I^-$
Synthesis	Reaction tube (~ 800 °C)	In solution (~ 100 °C)
Processing methods	sintering, sputtering	CVD, sputtering
Sample types	Powder, thin film	Single crystal, thin film
Typical band structures		
Band edge's main contribution	CBM X d/s VBM A p + B p	CBM B p VBM B s + X p
E_g (eV)	0.70-2.48	1.17-1.73
m_h (m_0)	0.26-0.98	0.14-0.31
E_b (meV)	4-65	14-68 ³⁷
Optical transition	Allowed	Allowed
Y (GPa)	90.10-181.48	17.79-21.92 ³⁸
Brittleness/Ductility	Brittleness	Ductility

Conclusion

In summary, we have studied the electronic, dielectric, and mechanical properties of cubic $Pm\bar{3}m$ phase antiperovskite X_3NA ($X^{2+} = Mg^{2+}, Ca^{2+}, Sr^{2+}$; $A^{3-} = P^{3-}, As^{3-}, Sb^{3-}, Bi^{3-}$) using

first-principles calculations. Similar to lead halide perovskites, the X_3NA has suitable band gaps (~ 1.5 eV), small carrier effective masses (0.26 - $0.98 m_0$), small exciton binding energies (4-65 meV), and allowed optical transitions at band edges. On the other hand, X_3NA exhibits totally different band edge characteristics, compared to the perovskites with electronically inverting the formula. The A-site ion has a non-negligible effect on the band edge character in the antiperovskites. Importantly, we find out a universal relationship between the tolerance factor and physical quantities, including band gap, Δ_{CBM} , average hole effective mass, valence band width, electronic dielectric constants, and Young's modulus. The linear relationship originates from the atomic orbital energy of X- and A-site element. This linear relationship has been further verified in antiperovskite $Mg_3NAs_{1-x}Bi_x$ alloys. Finally, we make a comprehensive comparison between the nitride-based antiperovskites and perovskites. Our work provides guidance for designing nitride antiperovskites for different applications.

Acknowledgement

This work is supported by the National Natural Science Foundation of China (Grant Nos. 11947218, 11704300), and the Natural Science Foundation of Hubei Province, China (2020CFA041). Guodong Yu acknowledges the support by the China Postdoctoral Science Foundation (Grant No. 2018M632902). Mao Yang acknowledge the support by China Scholarship Council Scholarship (No. 201908615047). Numerical calculations presented in this paper were performed on a supercomputing system in the Supercomputing Center of Wuhan University.

Author contributions

G.T. conceived the idea and designed the project. H.X.Z. carrier out most of the calculations and analyzed all data under S.J.Y.'s supervision. C.B.F. calculated the dielectric and mechanical properties. H.X.Z. and G.T. wrote the manuscript. S.J.Y. and G.T. revised the manuscript. All authors contributed to the discussion and revision of the paper.

References

1. Kim, J. Y.; Lee, J.-W.; Jung, H. S.; Shin, H.; Park, N.-G., High-efficiency perovskite solar cells. *Chem. Rev.* **2020**, *120* (15), 7867.
2. Tiwari, A.; Satpute, N. S.; Mehare, C. M.; Dhoble, S., Challenges, recent advances and improvements for enhancing the efficiencies of ABX_3 -based PeLEDs (perovskites light emitting diodes): A review. *J. Alloys Compd.* **2021**, *850* (0925), 156827.
3. Wang, H.; Kim, D. H., Perovskite-based photodetectors: materials and devices. *Chem. Soc. Rev.* **2017**, *46* (17), 5204.
4. Best Research-Cell Efficiency Chart. <https://www.nrel.gov/pv/assets/pdfs/best-research-cell-efficiencies:20200925:pdf>, Accessed October 3, 2020.
5. Kojima, A.; Teshima, K.; Shirai, Y.; Miyasaka, T., Organometal halide perovskites as visible-light sensitizers for photovoltaic cells. *J. Am. Chem. Soc.* **2009**, *131* (17), 6050.
6. Ju, M.-G.; Chen, M.; Zhou, Y.; Dai, J.; Ma, L.; Padture, N. P.; Zeng, X. C., Toward eco-friendly and stable perovskite materials for photovoltaics. *Joule* **2018**, *2* (7), 1231.
7. Li, H.; Wei, Q.; Ning, Z., Toward high efficiency tin perovskite solar cells: A perspective. *Appl. Phys. Lett.* **2020**, *117* (6), 060502.
8. Zhao, X.-G.; Yang, D.; Ren, J.-C.; Sun, Y.; Xiao, Z.; Zhang, L., Rational design of halide double perovskites for optoelectronic applications. *Joule* **2018**, *2* (9), 1662.
9. McCall, K. M.; Friedrich, D.; Chica, D. G.; Cai, W.; Stoumpos, C. C.; Alexander, G. C.; Deemyad, S.; Wessels, B. W.; Kanatzidis, M. G., Perovskites with a twist: strong In^{1+} off-centering in the mixed-valent $CsInX_3$ ($X=Cl, Br$). *Chem. Mater.* **2019**, *31* (22), 9554.
10. Slavney, A. H.; Leppert, L.; Bartesaghi, D.; Gold-Parker, A.; Toney, M. F.; Savenije, T. J.; Neaton, J. B.; Karunadasa, H. I., Defect-induced band-edge reconstruction of a bismuth-halide double perovskite for visible-light absorption. *J. Am. Chem. Soc.* **2017**, *139* (14), 5015.
11. Xiao, Z.; Du, K.-Z.; Meng, W.; Wang, J.; Mitzi, D. B.; Yan, Y., Intrinsic instability of $Cs_2In(I)M(III)X_6$ ($M= Bi, Sb$; $X= halogen$) double perovskites: a combined density functional theory and experimental study. *J. Am. Chem. Soc.* **2017**, *139* (17), 6054.
12. Swarnkar, A.; Mir, W. J.; Chakraborty, R.; Jagadeeswararao, M.; Sheikh, T.; Nag, A., Are chalcogenide perovskites an emerging class of semiconductors for optoelectronic properties and solar cell? *Chem. Mater.* **2019**, *31* (3), 565.
13. Sun, Q.; Yin, W.-J.; Wei, S.-H., Searching for stable perovskite solar cell materials using materials genome techniques and high-throughput calculations. *J. Mater. Chem. C* **2020**, *8* (35), 12012.
14. Niu, S.; Sarkar, D.; Williams, K.; Zhou, Y.; Li, Y.; Bianco, E.; Huyan, H.; Cronin, S. B.; McConney, M. E.; Haiges, R., Optimal bandgap in a 2D Ruddlesden–Popper perovskite chalcogenide for single-junction solar cells. *Chem. Mater.* **2018**, *30* (15), 4882.
15. Gebhardt, J.; Rappe, A. M., Adding to the perovskite universe: inverse-hybrid perovskites. *ACS Energy Lett.* **2017**, *2* (12), 2681.
16. Wang, Y.; Zhang, H.; Zhu, J.; Lü, X.; Li, S.; Zou, R.; Zhao, Y., Antiperovskites with exceptional functionalities. *Adv. Mater.* **2020**, *32* (7), 1905007.
17. Heinselman, K. N.; Lany, S.; Perkins, J. D.; Talley, K. R.; Zakutayev, A., Thin film synthesis of semiconductors in the Mg–Sb–N materials system. *Chem. Mater.* **2019**, *31* (21), 8717.
18. Dai, J.; Ju, M.-G.; Ma, L.; Zeng, X. C., $Bi(Sb)NCa_3$: Expansion of Perovskite Photovoltaics into All-Inorganic Anti-Perovskite Materials. *J. Phys. Chem. C* **2019**, *123* (11), 6363.
19. Gebhardt, J.; Rappe, A. M., Design of Metal-Halide Inverse-Hybrid Perovskites. *J. Phys. Chem. C*

2018, *122* (25), 13872.

20. Mochizuki, Y.; Sung, H.-J.; Takahashi, A.; Kumagai, Y.; Oba, F., Theoretical exploration of mixed-anion antiperovskite semiconductors M_3XN ($M= Mg, Ca, Sr, Ba$; $X= P, As, Sb, Bi$). *Phys. Rev. Mater.* **2020**, *4* (4), 044601.
21. Tang, G.; Xiao, Z.; Hong, J., Designing two-dimensional properties in three-dimensional halide perovskites via orbital engineering. *J. Phys. Chem. Lett.* **2019**, *10* (21), 6688.
22. Berger, R. F., Design principles for the atomic and electronic structure of halide perovskite photovoltaic materials: insights from computation. *Chem. Eur. J.* **2018**, *24* (35), 8708.
23. Zakutayev, A., Design of nitride semiconductors for solar energy conversion. *J. Mater. Chem. A* **2016**, *4* (18), 6742.
24. Ochi, M.; Kuroki, K., Comparative first-principles study of antiperovskite oxides and nitrides as thermoelectric material: multiple Dirac cones, low-dimensional band dispersion, and high valley degeneracy. *Phys. Rev. Appl.* **2019**, *12* (3), 034009.
25. Chi, E.; Kim, W.; Hur, N.; Jung, D., New Mg-based antiperovskites $PnNMg_3$ ($Pn= As, Sb$). *Solid State Commun.* **2002**, *121* (6-7), 309.
26. Zhao, Y.; Yu, P.; Zhang, G.; Sun, M.; Chi, D.; Hippalgaonkar, K.; Thong, J. T.; Wu, J., Low-Symmetry $PdSe_2$ for High Performance Thermoelectric Applications. *Adv. Funct. Mater.* **2020**, *30* (52), 2004896.
27. Chae, K.; Son, Y.-W., A New Family of Two-Dimensional Crystals: Open-Framework T_3X ($T= C, Si, Ge, Sn$; $X= O, S, Se, Te$) Compounds with Tetrahedral Bonding. *Nano Lett.* **2019**, *19* (4), 2694.
28. Raghuvanshi, P. R.; Mondal, S.; Bhattacharya, A., A high throughput search for efficient thermoelectric half-Heusler compounds. *J. Mater. Chem. A* **2020**, *8* (47), 25187.
29. Gibbs, Z. M.; Ricci, F.; Li, G.; Zhu, H.; Persson, K.; Ceder, G.; Hautier, G.; Jain, A.; Snyder, G. J., Effective mass and Fermi surface complexity factor from ab initio band structure calculations. *NPJ Comput. Mater.* **2017**, *3* (1), 1.
30. Linaburg, M. R.; McClure, E. T.; Majher, J. D.; Woodward, P. M., $Cs_{1-x}Rb_xPbCl_3$ and $Cs_{1-x}Rb_xPbBr_3$ Solid Solutions: Understanding Octahedral Tilting in Lead Halide Perovskites. *Chem. Mater.* **2017**, *29* (8), 3507.
31. Lee, J.-H.; Bristowe, N. C.; Lee, J. H.; Lee, S.-H.; Bristowe, P. D.; Cheetham, A. K.; Jang, H. M., Resolving the physical origin of octahedral tilting in halide perovskites. *Chem. Mater.* **2016**, *28* (12), 4259.
32. Ming, W.; Shi, H.; Du, M.-H., Large dielectric constant, high acceptor density, and deep electron traps in perovskite solar cell material $CsGeI_3$. *J. Mater. Chem. A* **2016**, *4* (36), 13852.
33. Han, D.; Shi, H.; Ming, W.; Zhou, C.; Ma, B.; Saparov, B.; Ma, Y.-Z.; Chen, S.; Du, M.-H., Unraveling luminescence mechanisms in zero-dimensional halide perovskites. *J. Mater. Chem. C* **2018**, *6* (24), 6398.
34. Takahashi, A.; Kumagai, Y.; Miyamoto, J.; Mochizuki, Y.; Oba, F., Machine learning models for predicting the dielectric constants of oxides based on high-throughput first-principles calculations. *Phys. Rev. Mater.* **2020**, *4* (10), 103801.
35. Dalpian, G. M.; Zhao, X.-G.; Kazmerski, L.; Zunger, A., Formation and composition-dependent properties of alloys of cubic halide perovskites. *Chem. Mater.* **2019**, *31* (7), 2497.
36. Tan, Y.; Chen, F. W.; Ghosh, A. W., First principles study and empirical parametrization of twisted bilayer MoS_2 based on band-unfolding. *Appl. Phys. Lett.* **2016**, *109* (10), 101601.

37. Yang, Z.; Surrente, A.; Galkowski, K.; Bruyant, N.; Maude, D. K.; Haghimirad, A. A.; Snaith, H. J.; Plochocka, P.; Nicholas, R. J., Unraveling the exciton binding energy and the dielectric constant in single-crystal methylammonium lead triiodide perovskite. *J. Phys. Chem. Lett.* **2017**, *8* (8), 1851.

38. Faghahnasiri, M.; Izadifard, M.; Ghazi, M. E., DFT study of mechanical properties and stability of cubic methylammonium lead halide perovskites ($\text{CH}_3\text{NH}_3\text{PbX}_3$, X= I, Br, Cl). *J. Phys. Chem. C* **2017**, *121* (48), 27059.